Anomalous thermal expansion in orthorhombic perovskite $SrIrO_3$: Interplay between spin-orbit coupling and the crystal lattice

Peter E. R. Blanchard, Emily Reynolds, and Brendan J. Kennedy*
School of Chemistry, The University of Sydney, Sydney, New South Wales 2006, Australia

Justin A. Kimpton
Australian Synchrotron, 800 Blackburn Road, Clayton, Victoria 3168, Australia

Maxim Avdeev
Bragg Institute, Australian Nuclear Science and Technology Organisation, Lucas Heights, New South Wales 2234, Australia

Alexei A. Belik
International Center for Materials Nanoarchitectonics (WPI-MANA), National Institute for Materials Science, 1-1 Namiki, Tsukuba, Ibaraki 305-0044, Japan

(Received 20 February 2014; revised manuscript received 11 May 2014; published 16 June 2014)

The structure of the orthorhombic (*Pbnm*) polytype of $SrIrO_3$ has been investigated between 3 and 1100 K using a combination of synchrotron and neutron diffraction methods. The orthorhombic structure persists to 1100 K, the highest temperature available in this work. This is a consequence of the larger than expected octahedral tilting estimated from the neutron diffraction studies. We postulate that the strong spin-orbit coupling of the Ir^{4+} cation, which splits the t_{2g} band, introduces additional strain on the lattice. This introduces unusual thermal expansion of the cell. $SrIrO_3$ was characterized by resistivity, magnetization, and specific heat measurements. Metallic conductivity was observed between 2 and 300 K without indication of the previously reported metal-insulator transition. The Sommerfeld constant γ was 3.12(2) mJ mol^{-1} K^{-2}, and a Fermi-liquid behavior was observed between 2 and 30 K with positive magnetoresistence of up to 2% (at 70 kOe and between 2 and 50 K).

DOI: 10.1103/PhysRevB.89.214106 PACS number(s): 61.05.fg, 61.66.Fn, 75.47.Lx

I. INTRODUCTION

Oxides containing 4*d* and 5*d* transition metal oxides that adopt a perovskite-type structure have attracted considerable attention in recent times as a consequence of their unexpected, and often exotic, electronic and magnetic behavior. Since the *d* orbitals of the 4*d* and 5*d* transition metal atoms are more extended than their 3*d* counterparts, their oxides are expected to exhibit weak electron correlations and relatively "normal" properties. Recent studies demonstrate this expectation is not always met, as illustrated, for example, by the unusual behavior of Sr_2IrO_4, which displays antiferromagnetic insulator properties [1], the giant magnetoelastic effect in $Ba_3BiIr_2O_9$ [2], and $SrTcO_3$, which displays an extraordinarily high Neel temperature [3]. Among the 4*d* and 5*d* oxides, those of iridium are of particular interest as a consequence of the emergence of novel electronic states associated with large spin-orbit coupling of the iridium cation [4–8].

The diversity of structures and properties exhibited by the alkaline earth iridium oxides $AIrO_3$, where A = Ca, Sr, or Ba, partially illustrates the importance of electron correlations. $BaIrO_3$ prepared at ambient pressure adopts a 9*R*-type perovskite structure and is a weak ferromagnetic semiconductor [9]. The notation 9*R*, developed by Katz and Ward [10], describes an *hhc* arrangement of the IrO_6 octahedra, where "*h*" describes hexagonal stacking of the face-sharing octahedra, and "*c*" is cubic-stacking corner-sharing octahedra. The ferromagnetism in $BaIrO_3$ originates from spin-orbit interactions, rather than the more typical spin canting [11]. High-pressure synthetic methods stabilize a number of polytypes of $BaIrO_3$, including a tetragonal structure in space group *I*4/*mcm*, which only contains corner-sharing octahedra [12]. This is the same structure adopted by $SrTiO_3$ at low temperatures [13]. When prepared at ambient pressure, $SrIrO_3$ has a monoclinic distorted six-layer (6H) $BaTiO_3$ (*hcc*) structure and is paramagnetic with metallic conductivity [14]. Quenching $SrIrO_3$ from high pressure and high temperature stabilizes the corner-sharing orthorhombic perovskite structure in space group *Pbnm* [15]. Conductivity measurements of this phase reveal that a transition from a bad metal to insulator occurs upon cooling. It has recently been shown that the orthorhombic structure can also be stabilized by chemical doping, forming oxides of the type $SrIr_{1-x}M_xO_3$ [16,17]. $CaIrO_3$ also forms an orthorhombic perovskite structure in *Pbnm*, when prepared using *chimie douce* methods [18]. This is Pauli paramagnetic metal. Conventional high-temperature methods yield a form with a unique orthorhombic structure in space group *Cmcm* that consists of layers of IrO_6 octahedra and is an antiferromagnetic insulator [19,20].

Although the room-temperature structures of many of the $AIrO_3$ perovskites are now well established, very little is known regarding their temperature dependence. High-resolution variable-temperature structural studies have emerged as a powerful means by which to probe coupling of electronic factors such as spin or orbital degrees of freedom with the lattice [21,22]. Combinations of these instabilities interact across phase transitions through elastic stresses and

*Corresponding author: Brendan.Kennedy@Sydney.edu.au

symmetry-allowed coupling invariants, as described within Landau theory. Such coupling can introduce anisotropic expansion of the unit cell parameters [23,24]. The use of such studies to study the impact of spin-orbit coupling on the lattice does not appear to have been considered. The fact that the orthorhombic form of $SrIrO_3$ can only be obtained through high-pressure synthetic methods has resulted in a paucity of studies of this unusual material. The aim of the present work is to establish the temperature dependence of the structure of $SrIrO_3$, seeking evidence for coupling between the lattice and electronic effects.

II. EXPERIMENTAL

The single-phase ambient-pressure modification of $SrIrO_3$ was prepared from a stoichiometric mixture of $SrCO_3$ and Ir by annealing in a Pt crucible under air at 1300 K for 48 h with two intermediate grindings. The high-pressure modification was obtained by the treatment of the ambient-pressure modification at 6 GPa and 1300 K for 1 h in Au capsules. The high-pressure modification of $SrIrO_3$ contained a trace amount of IrO_2 impurity, estimated to be ~0.04(2) weight percent by Rietveld refinement.

Magnetic susceptibilities ($\chi = M/H$) were measured using a pellet (about 0.4 g) on a superconducting quantum interference device (SQUID) magnetometer (Quantum Design, Magnetic Property Measurement System [MPMS]) between 2 and 300 K at 10 kOe under both zero-field-cooled (ZFC) and field-cooled (FC, on cooling) conditions. No sample holders were used (that is, the sample was put directly into a plastic straw), and no core diamagnetism correction was applied. Isothermal magnetization measurements were performed between −10 and 10 kOe at 5 K, and from 70 kOe to 0 Oe at 2 K. Specific heat, C_p, at magnetic fields of 0 and 90 kOe was recorded between 2 and 50 K on cooling by a pulse relaxation method using a commercial calorimeter (Quantum Design, Physical Property Measurement System [PPMS]). The dc electrical resistivity was measured between 2 and 300 K at 0 and 90 kOe by the conventional four-probe method using a Quantum Design PPMS with a dc-gauge current of 0.5 mA; magnetoresistance was measured between 0 and 70 kOe and 2 and 60 K with a current of 1 mA.

Neutron diffraction data for $SrIrO_3$ were collected over the angular range $10° < 2\theta < 162°$ with the wavelength 1.622 Å, using the high-resolution powder diffractometer Echidna at the Australian Nuclear Science and Technology Organisation's OPAL facility [25]. The wavelength was obtained using a Ge (335) monochromator. The powder sample (about 3 g) was loaded into a 6 mm vanadium can, and data were collected between 3 and 300 K, with temperature control being achieved through a closed-cycle cryostat.

Synchrotron x-ray powder diffraction data were collected using the powder diffractometer at beamline BL-10 of the Australian Synchrotron [26]. The wavelength was set at 0.58966 Å, and the precise value of this was determined using a NIST LaB_6 standard reference material. A finely ground sample was placed in a 0.2-mm-diameter quartz capillary that was rotated during the measurements. Temperature control was achieved using a Cyberstar hot-air blower and Oxford cryostream. Once the control sensor had reached the set point temperature, data collection commenced after a 3 min thermal equilibration period; thermal stability was of the order ±1.0 °C for all data collection temperatures. The data were measured for 5 min at each of the two detector settings and were collected with increasing temperatures.

The structures were refined by the Rietveld method using the General Structure Analysis System (GSAS) program. The peak shapes of both the synchrotron x-ray diffraction (S-XRD) and neutron powder diffraction (NPD) data were modeled using a pseudo-Voigt function, convoluted with the asymmetry in the NPD data that arises from axial divergence. Background was estimated by linear interpolation between ~30 background points. Both structural and profile parameters were varied during the refinement.

III. RESULTS AND DISCUSSION

The temperature dependence of the magnetic susceptibilities demonstrated $SrIrO_3$ to be a Pauli paramagnetic. The magnetic susceptibilities were essentially constant over a wide temperature range with an upturn evident at low temperatures due to the presence of paramagnetic impurities or defects (Fig. 1). There was no significant difference between the ZFC and FC curves.

The FC $\chi(T)$ susceptibilities were fit with the equation:

$$\chi(T) = \chi_0 + 0.125\mu_{\text{eff}}^2/(T - \theta_{\text{imp}}) + \alpha T^2 \qquad (1)$$

where χ_0 is the temperature-independent term that includes the diamagnetic and Pauli paramagnetic contributions, μ_{eff} is the magnetic moment of the impurity phase, and θ_{imp} is the impurity Curie-Weiss temperature. The αT^2 term is considered to originate from the higher-order temperature-dependent term in the Pauli paramagnetism, which is neglected in the zero-order approximation. This term reflects the shape of the density of

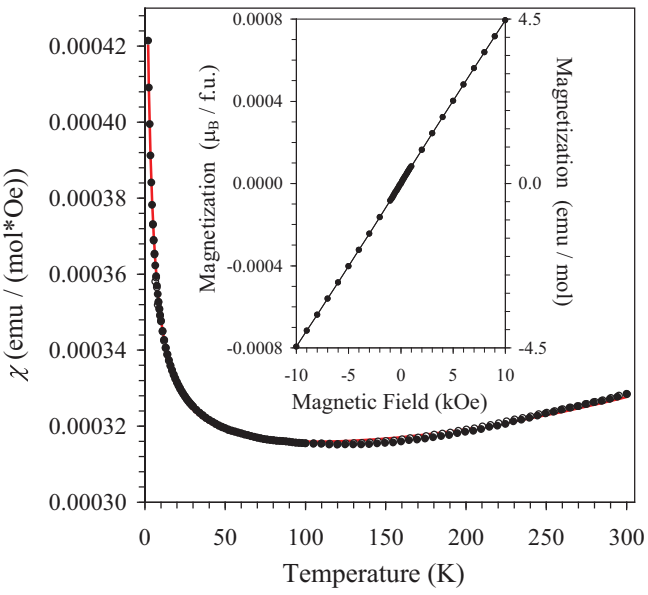

FIG. 1. (Color online) ZFC (white circles) and FC (black circles) dc magnetic susceptibility ($\chi = M/H$) curves of $SrIrO_3$ at 10 kOe. The line shows the fitting results with Eq. (1). The insert gives the isothermal magnetization curve at 5 K.

states at the Fermi level. A fit of (1) over the whole temperature range of 2–300 K resulted in $\chi_0 = 3.095(2) \times 10^{-4}$ cm^3/mol, $\mu_{\rm eff} = 0.0615(3)\ \mu_{\rm B}$, $\theta_{\rm imp} = -2.28(5)$ K, and $\alpha = 1.85(4) \times 10^{-10}$ cm^3 mol^{-1} K^{-2}. The $\mu_{\rm eff}$ of the impurity was about two times smaller than that reported by Zhao *et al.* [15]. The M vs H curve at 5 K is shown in the insert of Fig. 1; the curve was linear between −10 kOe and 10 kOe, in comparison with the results of Zhao *et al.* [15]. Almost linear behavior of the M vs H curve was observed at 2 K for applied magnetic fields of up to 70 kOe (with $M = 21$ emu/mol at 2 K and 70 kOe; the curve is not shown), in comparison with M vs H curves of 6H-$SrIrO_3$ at 2 K, where saturation behavior was observed [7].

The temperature dependence of resistivity at 0 and 90 kOe is shown on Fig. 2a. The present sample of $SrIrO_3$ exhibited metallic conductivity down to 2 K, indicating that it is a metal between 2 and 300 K. There is no indication of an upturn in resistivity below 50 K as described by Zhao *et al.* [15], suggesting that such behavior originates from boundary or impurity effects [14]. Application of an applied magnetic field of 90 kOe had very little effect on resistivity below about 100 K, with the values being almost within the experimental errors of measurements. Between 2 and 30 K, the temperature dependence of resistivity follows a T^2 law [Fig. 2(b)] indicating that $SrIrO_3$ is a typical Fermi-liquid metal. A positive magnetoresistence up to 2% (at 70 kOe and between 2 and 50 K) was observed [Fig. 2(c)]; magnetoresistence follows a H^2 law between about 0 and 30 kOe, confirming again that $SrIrO_3$ is a typical Fermi-liquid metal.

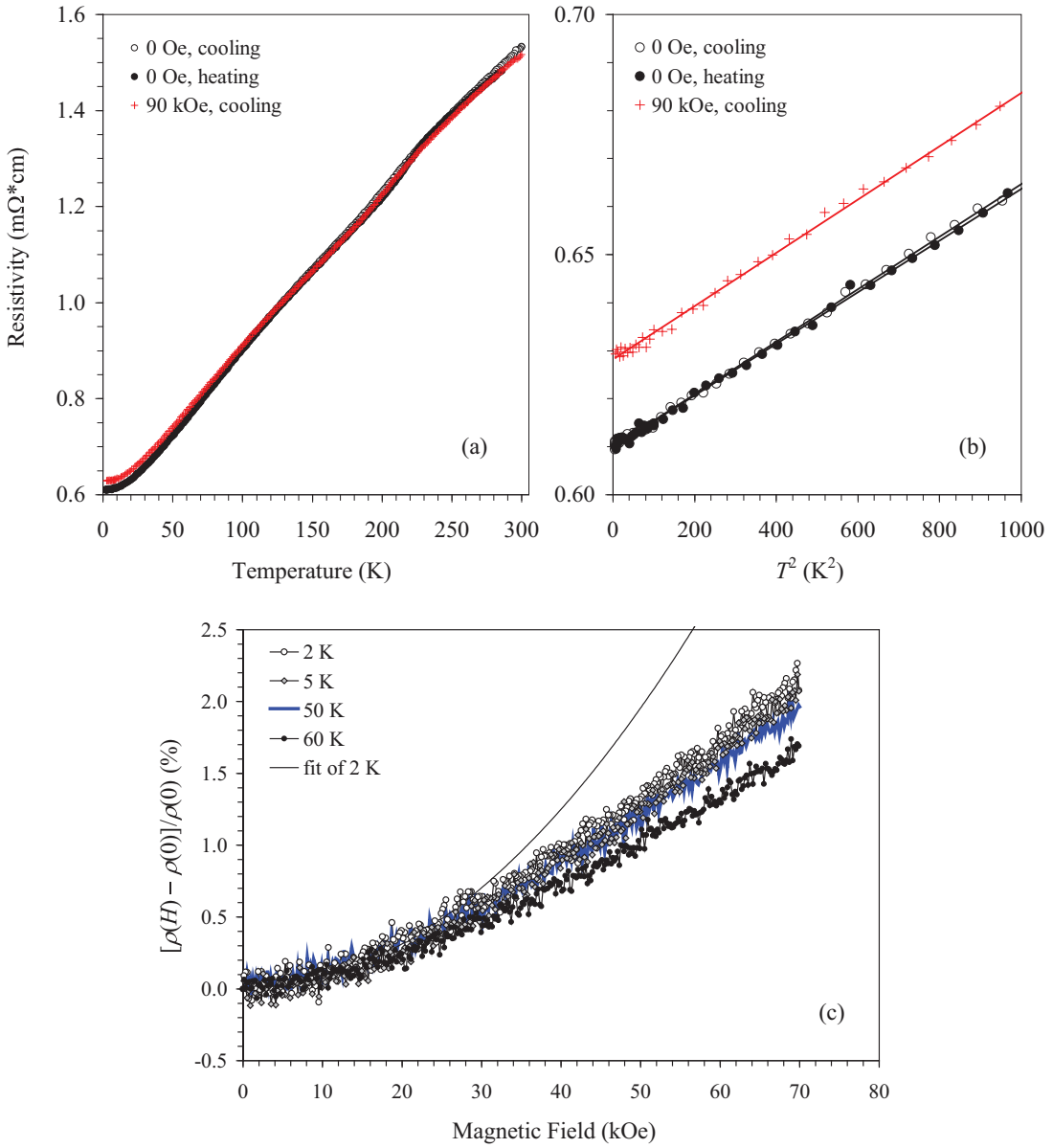

FIG. 2. (Color online) (a) Temperature dependence of resistivity of $SrIrO_3$ at 0 Oe on cooling and heating and at 90 kOe on cooling between 2 and 300 K. (b) The same curves plotted as ρ vs T^2 between 2 and 32 K. Lines give the least-square linear fits. (c) Magnetoresistance at different temperatures. The solid line shows the fit of the data at 2 K between 0 and 30 kOe with an H^2 law and highlights the variation at higher fields.

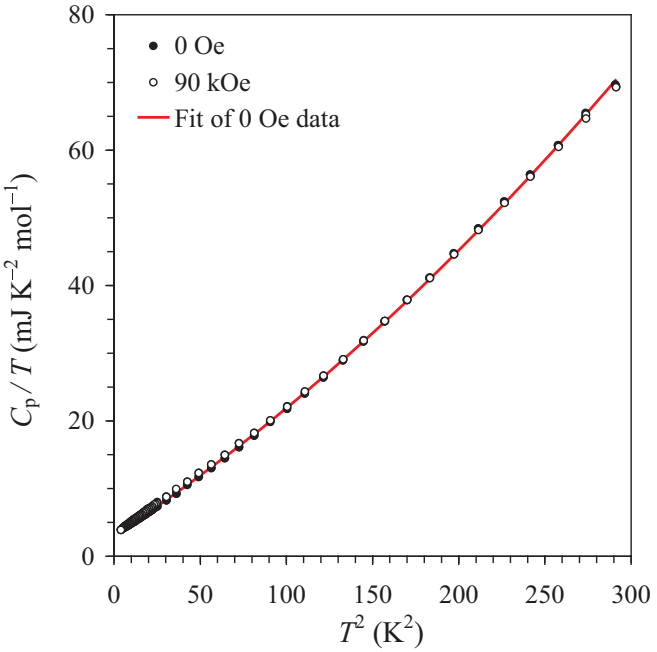

FIG. 3. (Color online) C_p/T vs T^2 curves of $SrIrO_3$ at 0 Oe (closed circles) and 90 kOe (open circles) between 2 and 17 K. The line shows the fitting results with Eq. (2).

Specific heat measurements at 0 and 90 kOe were essentially identical. The specific heat at 0 Oe between 2 and 17 K was fit by the equation (Fig. 3)

$$C_p(T) = \gamma T + \beta_1 T^3 + \beta_2 T^5 \qquad (2)$$

where the first term is associated with the electronic contribution, and the second and third terms describe the lattice contribution. The fitted parameters were $\gamma = 3.12(2)$ mJ mol^{-1} K^{-2}, $\beta_1 = 0.1648(6)$ mJ mol^{-1} K^{-4}, and $\beta_2 = 2.27(3) \times 10^{-4}$ mJ mol^{-1} K^{-6}. There were no anomalies in the Sommerfeld constant γ, and the value of this is comparable with that of metallic 6H-$SrIrO_3$ ($\gamma = 1.50$ mJ mol^{-1} K^{-2}). The γ values were significantly larger in semiconducting orthorhombic $SrIr_{0.75}Li_{0.25}O_3$ ($\gamma = 14.8$ mJ mol^{-1} K^{-2}) and $SrIr_{0.75}Zn_{0.25}O_3$ ($\gamma = 6.5$ mJ mol^{-1} K^{-2}) [16].

The S-XRD pattern for $SrIrO_3$, illustrated in Fig. 4, contains a number of weak reflections, associated with cooperative tilting of the corner-sharing IrO_6 octahedra. These reflections were more obvious in the corresponding neutron diffraction pattern. These peaks are associated with "frozen" phonon modes at particular points in the Brillouin zone corresponding to in-phase and out-of-phase rotations of the IrO_6 octahedra. For example, the in-phase tilts in the orthorhombic *Pbnm* structure, which has the Glazer tilt system ($a^-a^+c^+$) [27], are associated with the mode characterized by the $irrep M_3^+$, which condenses at the M point [$k = (1/2, 1/2, 0)$] of the Brillouin zone of the aristotype cubic perovskite, whereas the out-of-phase tilts are associated with the $irrep R_4^+$. The relatively weak scattering of x rays by oxygen anions, relative to that of iridium cations, reduces the intensity of the superlattice peaks, arising from octahedral rotation, which limits the accuracy with which the anion positions can be determined if XRD alone is used. Consequently, we used

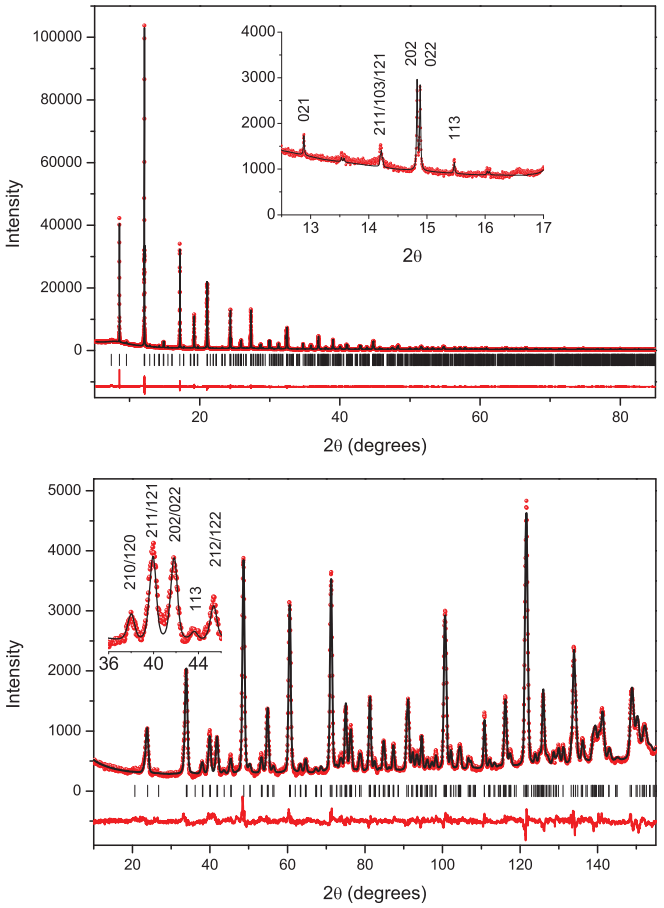

FIG. 4. (Color online) Observed, calculated, and difference data for S-XRD ($\lambda = 0.58966$ Å) and NPD ($\lambda = 1.6221$ Å) for $SrIrO_3$ at 300 K. The structure was refined in space group *Pbnm*. The inset in the S-XRD profiles shows the strongest superlattice reflections.

neutron diffraction to refine a precise and accurate structure of $SrIrO_3$. As evident from Fig. 4, the superlattice reflections are relatively stronger in the neutron diffraction pattern.

Both the synchrotron and neutron diffraction data were well fitted with an orthorhombic model in space group *Pbnm*. This orthorhombic structure is a $\sqrt{2}a_p \times \sqrt{2}b_p \times 2c$ supercell of the primitive perovskite of cell length a_p as a consequence of the octahedral rotations. The refined atomic positions for $SrIrO_3$ at 3 and 300 K are given in Table I. Refinements against the neutron diffraction data demonstrated both anion sites to be fully occupied, and we conclude the sample lacks appreciable amounts of anion vacancies.

The average Ir–O distance at 300 K of 2.016 Å is similar to that seen in Ir^{4+} oxides, such as $IrO_2 = 1.985$ Å [28] and $Bi_2Ir_2O_7 = 2.003$ Å [29]. The individual IrO_6 octahedra are relatively rigid, with the three crystallographically distinct Ir–O distances all being approximately equal (Table I). The bond valence sum (BVS) of the Ir cation is 4.03. The coordination of the Sr is reduced from 12, seen in the cubic $Pm\bar{3}m$ polytype, to 8, with the BVS for Sr being 2.24. The magnitude of the tilts can be estimated from the refined atomic coordinates. The orthorhombic *Pbnm* perovskite structure is characterized by two independent octahedral tilts, ψ and φ, where ψ is an out-of-phase tilt about the pseudocubic 110 axes, and φ is an

TABLE I. Refined atomic positions for $SrIrO_3$ at room temperature and at 3 K. The structures were refined in space group *Pbnm* against powder neutron diffraction data.

Temp (K)	300	3
R_p (%)	4.55	4.59
R_{wp} (%)	6.03	5.77
χ^2	2.31	2.51
a (Å)	5.60075(14)	5.58871(20)
b (Å)	5.57115(14)	5.57245(19)
c (Å)	7.89601(19)	7.88413(30)
Vol (Å^3)	246.376(11)	245.534(15)
Z	4	4
Sr x	−0.0068(8)	−0.0071(7)
y	0.4687(4)	0.46442(35)
U_{iso} $x100$ (Å^2)	1.97(4)	1.39(4)
Ir U_{iso} 100 (Å^2)	1.69(2)	1.45(2)
O1 x	0.0718(7)	0.0764(7)
y	0.0049(6)	0.0093(8)
U_{eqv} $x100$ (Å^2)	1.90*	1.50*
O2 x	0.2126(4)	0.2110(5)
y	0.2877(4)	0.2879(5)
z	−0.0369(4)	−0.0373(4)
U_{eqv} $x100$ (Å^2)	2.15*	1.60*
Ir–O(1) (Å)	2.0148(8)	2.0174(9)
Ir–O(2) (Å)	2.018(2)	2.023(3)
	2.018(3)	2.013(3)

*Anisotropic displacement parameters were refined for the anions. In space group *Pbnm*, the Sr cations are on 4*c* sites at *x y* 1/4, the Ir cations are on the 4*a* sites at 0 0 0, and O1 on 4*c* sites at *x y* 1/4 and O2 on 8*d* sites at *x y z*.

in-phase tilt about the pseudocubic 001 axis, and the magnitude of these can be estimated from the displacement of the O2 oxygen atoms from (¼ ¼ 0) to (¼-u ¼+v w) [30]. The out-of-phase tilting is given by $\tan\psi = 4\delta$, where $\delta = \frac{u+v}{2}$. The in-phase tilt is calculated as the average of $\tan\varphi = 4\sqrt{2}w$ and $\tan\varphi = 2\sqrt{2}x$, where x is the coordinate of the O1anions [31]. For $SrIrO_3$, we find the in-phase tilts to be 8.7° and out-of-phase tilts to be 11.5° at 300 K. These values are somewhat larger than those found for the related 4*d* oxide $SrRuO_3$, which has tilts of 6.5° and 7.6° [32,33]. This difference is somewhat surprising since the crystal chemistry of Ru and Ir oxides is generally considered to be very similar, reflecting the similarity in the ionic radii of Ru^{4+} and Ir^{4+}, 0.620 vs 0.625 Å, respectively [34]. The tilt angles in $SrIrO_3$ are essentially independent of temperature below 300 K (see Fig. 5). The use of x-ray data for the high-temperature measurements precludes an accurate estimation of tilts above 300 K.

The tolerance factors (t), expressed as $t = (r_A + r_O)/\sqrt{2}(r_B + r_O)$, where r_A, r_B, and r_O are ionic radii of the respective ions, for $SrRuO_3$ and $SrIrO_3$ are essentially identical, 0.9942 vs 0.9917, respectively. Consequently, it might be expected that $SrIrO_3$ would undergo the same sequence of phase transitions seen for $SrRuO_3$. As evident from Fig. 5, this is not the case. Rather, the orthorhombic *Pbnm* structure persists over the temperature range 3–1070 K, whereas $SrRuO_3$ becomes cubic when heated above ~950 K, with intermediate transitions to orthorhombic

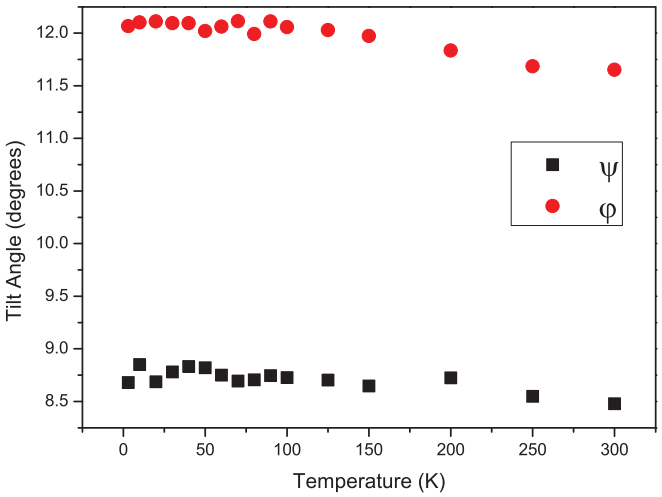

FIG. 5. (Color online) Temperature dependence of the in-phase (ψ) and out-of-phase (φ) tilts for $SrIrO_3$ estimated from the atomic coordinates of the anions refined against the powder neutron diffraction data.

and tetragonal forms at 685 and 825 K, respectively [32,33]. While unexpected, based on the tolerance factors, this difference in behavior is undoubtedly a consequence of the larger tilts observed in $SrIrO_3$. By comparison, $CaRuO_3$, which has a smaller tolerance factor $t = 0.9591$, remains orthorhombic to at least 1573 K [35], reflecting the larger tilt angles of ~11° and 15° at 300 K. A small number of weak additional reflections emerged as the sample was heated above 1020 K, and these persisted upon recooling the sample to room temperature (Fig. 6). Evidently, the sample is stable to ~1000 K but undergoes decomposition above this [14]. There is no evidence from the diffraction data for broadening of the diffraction peaks, either upon heating or upon recooling, with

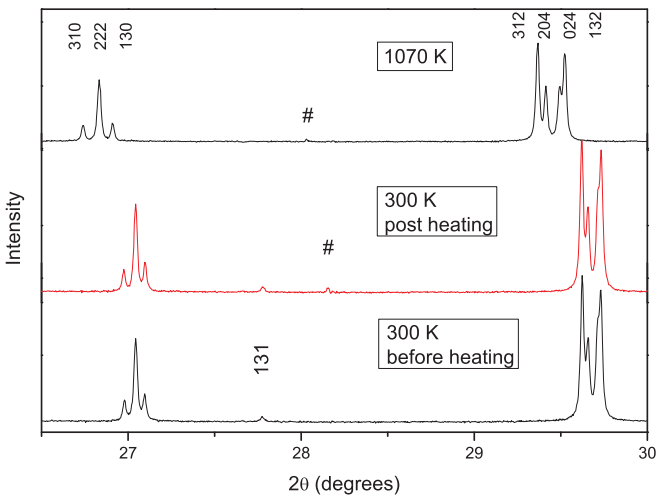

FIG. 6. (Color online) Portions of S-XRD profiles for $SrIrO_3$ obtained at 300 K before heating the sample to 1070 K and then at 300 K after recooling the sample. The presence of a weak peak that forms above ~1000 K is indicated (#). The data were collected at $\lambda = 0.8255$ Å.

the changes in Fig. 6 attributed to the anisotropic nature of the thermal expansion.

Recall that the more the tolerance factor is reduced below unity, the larger the octahedral tilting will be at room temperature and the higher the temperature of the transition to cubic will be. As illustrated by Knight in his studies of isostructural $CaTiO_3$ [37] and $LaGaO_3$ [38], if no additional factors are present, both the unit cell volume and the individual lattice parameters will show relatively simple thermal expansion at temperatures well below a ferroelastic transition temperature. This also appears to be the case for $CaRuO_3$, where the temperature dependence of the lattice parameters was fitted using a simple quadratic expression [35]. The thermal variation in the unit cell volume for $SrIrO_3$ is shown in Fig. 7 and exhibits the expected behavior: saturation at the lowest temperature

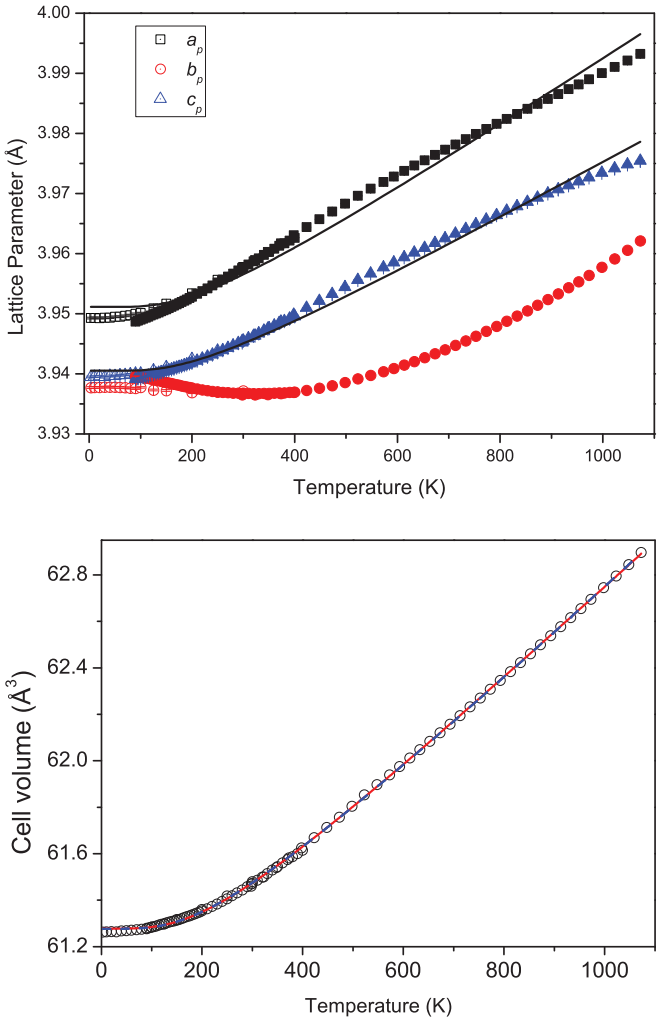

FIG. 7. (Color online) The temperature dependence of the unit cell parameters and volume (V/Z) of $SrIrO_3$. For clarity, the orthorhombic unit cell parameters are shown as their primitive equivalents $a/\sqrt{2} \times b/\sqrt{2} \times c/2$. Where not apparent, the esds are smaller than the symbols. The fit to the reduced unit cell volume of $SrIrO_3$ to the first- and second-order Grüneisen approximation is shown as the red and blue lines, respectively. The solid line for the individual lattice parameters is $a_0 = a_1 + a_2 \coth(\frac{\theta_s}{T})$, where θ_s is the saturation temperature for the thermal expansion [36].

and a constant thermal expansion coefficient at the highest temperatures studied. The thermal expansion of the volume was analyzed using the Grüneisen model for the zero-pressure equation of state. The approximations of both first and second order, having the forms $V(T) = V0 + \frac{\gamma \cdot U}{K0}$ and $V(T) = V0 + \frac{V0 \cdot U}{Q - b \cdot U}$, respectively [39], were tested, where $V0$ is the unit cell volume at $T = 0$ K, γ is a temperature-independent Grüneisen parameter, $Q = \frac{V0 \cdot K0}{\gamma}$, $b = (K0' - 1)/2$, $K0$ and $K0'$ are the bulk modulus and its first pressure derivative, respectively, and U is the internal energy expressed according to the Debye model as:

$$U(T) = 9Nk_BT\left(\frac{T}{\theta_D}\right)^3 \int_0^{T/\theta_D} \frac{x^3}{e^x - 1} dx, \qquad (3)$$

where N is the number of atoms in the unit cell, k_B is the Boltzmann constant, and θ_D is the Debye temperature.

The least-squares minimization with numerical integration produced nearly identical fit quality and parameter values for both first- and second-order approximations (Fig. 7): reduced $\chi^2 = 3.634 \times 10^{-5}$, $V0 = 61.277(1)$ Å^3, $\gamma/K0 = 9.74(3) \times 10^{-12}$ Pa^{-1}, $\theta_D = 806(7)$ K, and $\chi^2 = 3.614 \times 10^{-5}$, $V0 = 61.276(1)$ Å^3, $Q = 6.41(9) \times 10^{-18}$ J, $\gamma/K0 = 9.57(3) \times 10^{-12}$ Pa^{-1}, $b = 0.5(4)$, $\theta_D = 791(14)$ K, respectively. Since the individual cell parameters clearly display non-Grüneisen behavior, the parameter values except $V0$ should be taken only as a crude estimate. The derived Debye temperature is somewhat higher than that previously reported for orthorhombic $SrIrO_3$ based on heat capacity data analysis, 556 K [18], but the Q and b parameters are close to the values reported for other perovskites [38,40]. Given that a typical value of bulk modulus for oxides falls into a 150–250 GPa range, we can estimate the Grüneisen parameter value at $T = 0$ to be ~1.4–2.4, which is very close to the values typically found in ABO_3 perovskites [37].

The spin-orbit interaction plays a crucial role in the magneto-conductivity of $SrIrO_3$ [41]. While this may contribute to the observed discrepancy between the observed and calculated saturation behavior, the difference appears to begin at somewhat higher temperatures. This is reflected in the thermal expansion of the individual unit cell parameters, and, as is evident from Fig. 7, none of the individual lattice parameters displays simple thermal expansion behavior. Proximity to a ferroelastic structural phase transition is known to modify the high-temperature thermal expansion of metal oxides. Likewise, magnetic transition can result in anisotropic thermal expansion. Clearly, neither of these effects is active here. Unfortunately, it was not possible to obtain precise structures from the high-temperature S-XRD due to the relatively low scattering factor of oxygen. Reexamination of the thermal expansion of 6H-$SrIrO_3$ described previously shows that it displays typical behavior [16].

The initial question then becomes: Why is the effective tolerance factor in $SrIrO_3$ smaller than that calculated based on the tabulated values of ionic radii? A further question is, what effect could impact on the anisotropic thermal expansion of the cell?

In addressing these questions, we initially recall that the tolerance factor, essentially, assumes ionic bonding, and that electrostatic interactions are the primary forces. Other factors,

including electronic effects, such as orbital ordering, and magnetic ordering, can impact on the local and average structures. Disorder can also impact the tilting; for example, anion vacancies tend to relieve underbonding of the *A*-site cations, reducing the need for tilting. Disorder appears not to be responsible for the anomalous behavior of $SrIrO_3$, since not only do we find no evidence for appreciable anion vacancies from the neutron diffraction analysis, but the tilts are actually greater in $SrIrO_3$ and not decreased as occurs in disordered perovskites such as Ba_2YTaO_6 or $Sr_2SrSbO_{5.5}$ [42,43].

It is possible that displacive disorder of the larger Sr cation could impact on the tilting. This is important in ferroelectric oxides such as $Pb(Zr_{1-x}Ti_x)O_3$, where the Pb^{2+} $6s^2$ lone pair electrons increase the energy of the Pb cations at the 1/2 0 0 site of the *Pm3m* structure [44]. This energy increase is reduced by allowing the cations to move away from the high-symmetry sites. Such disorder is often identified by anomalously large atomic displacement parameters. Again, the structural studies argue against this being the case here.

This suggests another mechanism is responsible for the increase in the tilt angles in $SrIrO_3$. Cheng *et al.* [12] recently noted that the effective tolerance factor in the high-pressure (*I*4/*mcm*) polytype of $BaIrO_3$ is smaller than expected based on the tabulated values for ionic radii, and they suggested this is a consequence of a change in the $5d\pi^*$ bands of the IrO_6 octahedra. The estimated tolerance factor for $BaIrO_3$ is 1.051, and the BVS for the Ba is estimated to be 2.56; such overbonding is not expected to be relieved by tilting. Spin-orbit coupling splits the formal t_{2g} manifold into a low-lying fully filled $J_{\text{eff}} = 3/2$ quadruplet and an excited half-filled $J_{\text{eff}} = 1/2$ doublet. In Ir^{4+} oxides, the spin-orbit splitting is sufficiently large to reduce the bandwidth of the $J = 1/2$ bands, inducing magnetism. Cheng *et al.* argue that the high-pressure conditions required to form the *I*4/*mcm* structure induce a change in the $J_{\text{eff}} = 3/2$ and 1/2 bands that acts to reduce the Ba–O equilibrium distance, and hence tolerance factor. Although the conditions used to prepare the present sample of $SrIrO_3$ were less extreme, 6 vs 25 GPa, it is reasonable to propose that the same effect is present. When prepared at 17 GPa, the related oxide $BaOsO_3$ adopts the cubic *Pm*3*m* structure [45]; the absence of any tilting is as expected based on the tolerance factor ($t = 1.049$) calculated from the tabulated ionic radii.

The postulate is then that spin-orbit coupling acts to alter the nature of the Ir–O bonding, thereby decreasing the effective tolerance factor and increasing the magnitude of the octahedral tilting, which in turn inhibits the transformation to a cubic structure. Spin-orbit coupling is also believed to play a role in the anomalous rate of thermal expansion of the individual lattice parameters as illustrated in Fig. 7. As evident from studies of the spin glass $Sr_{0.70}Ce_{0.30}MnO_3$ [46], subtle short-range magnetic ordering effects can induce strains in the lattice parameters. We speculate that the splitting of the t_{2g} band, introduced by the strong spin-orbit coupling of the Ir^{4+} cation, introduces additional strain on the lattice, and this is reflected in the thermal expansion.

IV. CONCLUSION

In closing, the structure of the orthorhombic (*Pbnm*) polytype of $SrIrO_3$ has been investigated between 3 and 1100 K using a combination of synchrotron and neutron diffraction methods. The fact that the orthorhombic structure persists to 1100 K, the highest temperature available in this work, is surprising based on the tolerance factor estimated from the ionic radii of the cations, but it is consistent with the magnitude of the octahedral tilting estimated from the neutron diffraction studies. It appears that the high-pressure conditions used to prepare $SrIrO_3$ induce a change in the $J_{\text{eff}} = 3/2$ and 1/2 bands that acts to reduce the Sr–O equilibrium distance, and hence tolerance factor. We postulate that the strong spin-orbit coupling of the Ir^{4+} cation, which splits the t_{2g} band, introduces additional strain on the lattice that results in the unusual thermal expansion of the cell.

ACKNOWLEDGMENTS

This work was, in part, performed at the Powder Diffraction Beamline at the Australian Synchrotron. We acknowledge the Australian Research Council (Grant No. DP110102662) and the Australian Institute for Nuclear Science and Engineering for financial support. A.A.B. acknowledges World Premier International Research Center Initiative (WPI Initiative, Ministry of Education, Culture, Sports, Science, and Technology, Japan), the Japan Society for the Promotion of Science (JSPS) through its "Funding Program for World-Leading Innovative R&D on Science and Technology (FIRST Program)," and the Grants-in-Aid for Scientific Research (22246083) from JSPS, Japan.

[1] G. Cao, J. Bolivar, S. McCall, J. E. Crow, and R. P. Guertin, Phys. Rev. B **57**, R11039 (1998).

[2] W. Miiller, M. Avdeev, Q. D. Zhou, B. J. Kennedy, N. Sharma, R. Kutteh, G. J. Kearley, S. Schmid, K. S. Knight, P. E. R. Blanchard, and C. D. Ling, J. Am. Chem. Soc. **134**, 3265 (2012).

[3] E. E. Rodriguez, F. Poineau, A. Llobet, B. J. Kennedy, M. Avdeev, G. J. Thorogood, M. L. Carter, R. Seshadri, D. J. Singh, and A. K. Cheetham, Phys. Rev. Lett. **106**, 067201 (2011).

[4] J.-M. Carter, V. V. Shankar, M. A. Zeb, and H.-Y. Kee, Phys. Rev. B **85**, 115105 (2012).

[5] K. Ohgushi, J.-i. Yamaura, H. Ohsumi, K. Sugimoto, S. Takeshita, A. Tokuda, H. Takagi, M. Takata, and T.-h. Arima, Phys. Rev. Lett. **110**, 217212 (2013).

[6] M. A. Zeb and H.-Y. Kee, Phys. Rev. B **86**, 085149 (2012).

[7] G. Cao, V. Durairaj, S. Chikara, L. E. DeLong, S. Parkin, and P. Schlottmann, Phys. Rev. B **76**, 100402 (2007).

[8] H. Watanabe, T. Shirakawa, and S. Yunoki, Phys. Rev. Lett. **110**, 027002 (2013).

[9] G. Cao, J. E. Crow, R. P. Guertin, P. F. Henning, C. C. Homes, M. Strongin, D. N. Basov, and E. Lochner, Solid State Commun. **113**, 657 (2000).

[10] L. Katz and R. Ward, Inorg. Chem. **3**, 205 (1964).
[11] M. A. Laguna-Marco, D. Haskel, N. Souza-Neto, J. C. Lang, V. V. Krishnamurthy, S. Chikara, G. Cao, and M. van Veenendaal, Phys. Rev. Lett. **105**, 216407 (2010).
[12] J. G. Cheng, T. Ishii, H. Kojitani, K. Matsubayashi, A. Matsuo, X. Li, Y. Shirako, J. S. Zhou, J. B. Goodenough, C. Q. Jin, M. Akaogi, and Y. Uwatoko, Phys. Rev. B **88**, 205114 (2013).
[13] G. Shirane and Y. Yamada, Phys. Rev. **177**, 858 (1969).
[14] J. M. Longo, J. A. Kafalas, and R. J. Arnott, J. Solid State Chem. **3**, 174 (1971).
[15] J. G. Zhao, L. X. Yang, Y. Yu, F. Y. Li, R. C. Yu, Z. Fang, L. C. Chen, and C. Q. Jin, J. Appl. Phys. **103**, 103706 (2008).
[16] I. Qasim, B. J. Kennedy, and M. Avdeev, J. Mater. Chem. A **1**, 3127 (2013).
[17] M. Bremholm, C. K. Yim, D. Hirai, E. Climent-Pascual, Q. Xu, H. W. Zandbergen, M. N. Ali, and R. J. Cava, J. Mater. Chem. **22**, 16431 (2012).
[18] J. G. Cheng, J. S. Zhou, J. B. Goodenough, Y. Sui, Y. Ren, and M. R. Suchomel, Phys. Rev. B **83**, 064401 (2011).
[19] K. Niwa, T. Yagi, K. Ohgushi, S. Merkel, N. Miyajima, and T. Kikegawa, Phys. Chem. Miner. **34**, 679 (2007).
[20] C. D. Martin, R. I. Smith, W. G. Marshall, and J. B. Parise, Am. Mineral. **92**, 1912 (2007).
[21] M. A. Carpenter, C. J. Howard, B. J. Kennedy, and K. S. Knight, Phys. Rev. B **72**, 024118 (2005).
[22] C. J. Howard, Z. Zhang, M. A. Carpenter, and K. S. Knight, Phys. Rev. B **76**, 054108 (2007).
[23] M. A. Carpenter and E. K. H. Salje, Eur. J. Mineral. **10**, 693 (1998).
[24] M. A. Carpenter, E. K. H. Salje, and A. Graeme-Barber, Eur. J. Mineral. **10**, 621 (1998).
[25] K. D. Liss, B. Hunter, M. Hagen, T. Noakes, and S. Kennedy, Physica B Condens. Matter **385-386**, 1010 (2006).
[26] K. S. Wallwork, B. J. Kennedy, and D. Wang, AIP Conf. Proc. **879**, 879 (2007).
[27] A. M. Glazer, Acta Crystallogr. B-Struct. Commun. **B 28**, 3384 (1972).
[28] A. A. Bolzan, C. Fong, B. J. Kennedy, and C. J. Howard, Acta Crystallogr. B-Struct. Commun. **53**, 373 (1997).
[29] B. J. Kennedy, J. Solid State Chem. **123**, 14 (1996).
[30] B. J. Kennedy, C. J. Howard, and B. C. Chakoumakos, J. Phys.-Condens. Matter **11**, 1479 (1999).
[31] B. J. Kennedy, I. Qasim, E. Reynolds, T.-Y. Tan, and Q. Zhou, Austr. J. Chem. **65**, 229 (2012).
[32] B. J. Kennedy and B. A. Hunter, Phys. Rev. B **58**, 653 (1998).
[33] B. J. Kennedy, B. A. Hunter, and J. R. Hester, Phys. Rev. B **65**, 224103 (2002).
[34] R. D. Shannon, Acta Crystallogr. A **32**, 751 (1976).
[35] R. Ranjan, A. Senyshyn, V. Vashook, R. Niewa, H. Boysen, and F. Frey, Appl. Phys. Lett. **90**, 251913 (2007).
[36] E. Salje, B. Wruck, and H. Thomas, Z. Physik B Condens. Matter **82**, 399 (1991).
[37] K. S. Knight, J. Alloys Compd. **509**, 6337 (2011).
[38] K. S. Knight, J. Solid State Chem. **194**, 286 (2012).
[39] D. C. Wallace, *Thermodynamics of Crystals* (Dover, New York, 1998).
[40] K. S. Knight and N. Bonanos, Solid State Ionics **232**, 112 (2013).
[41] F. X. Wu, J. Zhou, L. Y. Zhang, Y. B. Chen, S. T. Zhang, Z. B. Gu, S. H. Yao, and Y. F. Chen, J. Phys.-Condens. Matter **25**, 125604 (2013).
[42] Q. D. Zhou, B. J. Kennedy, and J. A. Kimpton, J. Solid State Chem. **184**, 729 (2011).
[43] Q. D. Zhou, B. J. Kennedy, and M. Avdeev, J. Solid State Chem. **184**, 2559 (2011).
[44] I. M. Reaney, D. I. Woodward, and C. A. Randall, J. Am. Ceram. Soc. **94**, 2242 (2011).
[45] Y. G. Shi, Y. F. Guo, Y. C. Shirako, W. Yi, X. Wang, A. A. Belik, Y. Matsushita, H. L. Feng, Y. Tsujimoto, M. Arai, N. L. Wang, M. Akaogi, and K. Yamaura, J. Am. Chem. Soc. **135**, 16507 (2013).
[46] Z. M. Zhang, B. J. Kennedy, C. J. Howard, M. A. Carpenter, W. Miiller, K. S. Knight, M. Matsuda, and M. Miyake, Phys. Rev. B **85**, 174110 (2012).